

## RESEARCH ARTICLE

10.1002/2013JB010564

## Key Points:

- Bookshelf faulting near Ziarat, Pakistan

## Supporting Information:

- Readme
- Figure S1

## Correspondence to:

B. Pinel-Puysségur,  
beatrice.puysegur@cea.fr

## Citation:

Pinel-Puysségur, B., R. Grandin, L. Bollinger, and C. Baudry (2014), Multifaulting in a tectonic syntaxis revealed by InSAR: The case of the Ziarat earthquake sequence (Pakistan), *J. Geophys. Res. Solid Earth*, 119, doi:10.1002/2013JB010564.

Received 29 JUL 2013

Accepted 30 MAY 2014

Accepted article online 4 JUN 2014

## Multifaulting in a tectonic syntaxis revealed by InSAR: The case of the Ziarat earthquake sequence (Pakistan)

B. Pinel-Puysségur<sup>1</sup>, R. Grandin<sup>2</sup>, L. Bollinger<sup>1</sup>, and C. Baudry<sup>1,3</sup>

<sup>1</sup>CEA, DAM, DIF, Arpajon Cedex, France, <sup>2</sup>IPGP, Paris, France, <sup>3</sup>Now at Safran Morpho, Issy-les-Moulineaux, France

**Abstract** On 28–29 October 2008, within 12 h, two similar  $M_w = 6.4$  strike-slip earthquakes struck Baluchistan (Pakistan), as part of a complex seismic sequence. Interferometric Synthetic Aperture Radar (InSAR) data reveal that the peak of surface displacement is near the Ziarat anticline, a large active fold affected by Quaternary strike-slip faulting. All coseismic interferograms integrate the deformation due to both earthquakes. As their causative faults ruptured close to each other, the individual signals cannot be separated. According to their focal mechanisms, each earthquake may have activated a NE-SW sinistral or a NW-SE dextral fault segment, which leads to four possible scenarios of fault orientations. A nonlinear inversion of the InSAR data set allows rejecting two scenarios. The best slip distributions on the two fault segments for the two remaining scenarios are determined by linear inversion. Stress-change modeling favors a scenario involving two abutting conjugate strike-slip faults. Two other fault segments accommodated left-lateral strike slip during the seismic sequence. The activated fault system includes multiple fault segments with different orientations and little surface expression. This may highlight, at a smaller scale, the distributed, possibly transient character of deformation within a broader right-lateral shear zone. It suggests that the activated faults delineate a small tectonic block extruding and subtly rotating within the shear zone. It occurs in the vicinity of the local tectonic syntaxis where orogenic structures sharply turn around a vertical axis. These mechanisms could participate in the long-term migration of active tectonic structures within this kinematically unstable tectonic syntaxis.

### 1. Introduction

The Indian plate converges at about 4 cm/yr relative to Eurasia, half of the motion being accommodated by shortening across the Himalayas [e.g., *Bettinelli et al.*, 2006] (Figure 1). On the western edge of the subcontinent, more than half of the motion relative to Afghanistan is taken up by the Chaman fault, a major sinistral strike-slip fault [e.g., *Molnar and Tapponnier*, 1975]. Most of the remaining motion between the Indian plate and Afghanistan is accommodated eastward within the Baluchistan fold and thrust belt (Figure 1), generating moderate to large earthquakes. Among them, three earthquakes occurred in the 1930s: the Sharig ( $M_w = 6.8$ ) and Mach ( $M_w = 7.3$ ) earthquakes in 1931, followed by the devastating 1935 Quetta great earthquake ( $M_w = 7.7$ ) that caused 35,000 deaths [West, 1934; *Quittmeyer and Jacob*, 1979; *Ambraseys and Bilham*, 2003; *Szeliga et al.*, 2009]. Recently, on 24 September 2013, another great earthquake ( $M_w = 7.7$ ) occurred to the southwest in Baluchistan [Avouac et al., 2014].

The Quetta region was affected by two  $M_w = 6.4$  earthquakes on 28 October 2008 at 23:59 UTC and on 29 October at 11:32 (i.e., 12 h afterward). Both earthquakes are characterized by very similar waveforms and strike-slip focal mechanisms. They are denoted EQ2 and EQ3 in Table 1 and Figure 2. These earthquakes were preceded by a  $M_w = 5.4$  event (EQ1) 35 min before the first shock. They were followed by a cluster of 47 aftershocks with magnitudes larger than 3.5. The events are located by global seismological networks within a large area, spreading over a 1500 km<sup>2</sup> region (source International Seismological Centre (ISC), U.S. Geological Survey (USGS)). The main shocks damaged a large area in the Karezat and Ziarat districts, destroyed several villages (MMI = VIII, total collapse of the mud houses), affected more than 120,000 people, and caused more than 160 deaths [Maqsood and Schwarz, 2010].

Several active faults were previously surveyed within 30 km of the main shock epicentral area, such as the Pishin, Gwal, Churmian, and Balozai faults [Nakata et al., 1991] (Figures 1 and 2). Some of these NE trending structures exhibit left-lateral strike-slip offsets. Farther east, activity of the conjugate NNW trending right-lateral strike-slip Urghargai fault system has also been suggested [Kazmi, 1979] (Figure 2). The local active

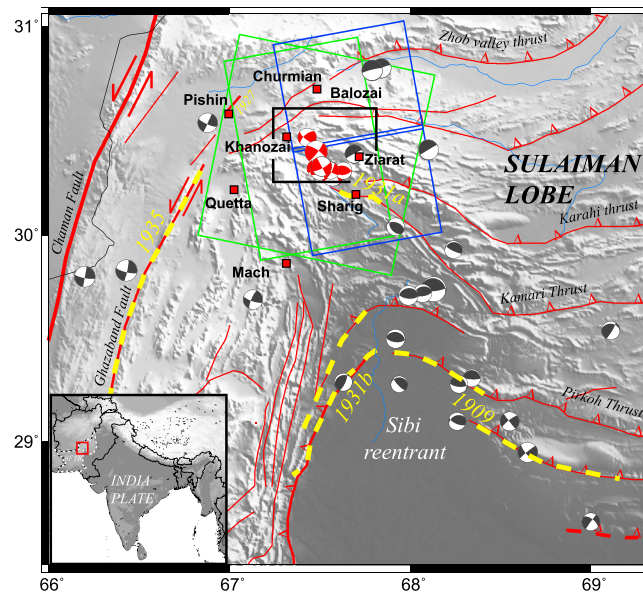


**Figure 1.** Topography and major tectonic features of the Sibi reentrant between the Kirthar and Sulaiman mountain ranges in Pakistan. The white dashed line and BFTB on inset refer to the Baluchistan Fold and Thrust Belt. Faults are from Bannert et al. [1995] and focal mechanisms from the global CMT catalogue. Yellow dashed lines and associated dates are the suspected ruptures of the largest historical earthquakes. Green and blue boxes are respectively the scene frames for the Envisat ASAR and ALOS PALSAR images used in this study. Black box is the frame of Figures 2, 9, and 10.

tectonic setting therefore appears complex: The deformation seems distributed on several structures with concurrent activity. This complexity is not surprising given the considerable strain partitioning accommodated in the whole region, from the Chaman fault to the west to the Sulaiman lobe and the Kirthar range [Haq and Davis, 1997; Bernard et al., 2000; Szeliga et al., 2012]. The focal mechanisms determined for the main shocks and the largest aftershocks of the 2008 sequence are consistent with the activation of either one nodal plane or the other. Nevertheless, no clear coseismic surface breaks were mapped on any of those structures in the field [PMD report, 2009]. Furthermore, the uncertainties on the absolute location of the earthquakes and their aftershocks precluded their association with one structure in particular. Given this indeterminacy, the previous studies on the 2008 earthquakes [McCloskey and Nalbant, 2009; Lisa and Jan, 2010; Yadav et al., 2012] located the seismogenic faults based on the earthquake epicenter

locations only. Without further constraints on the geometry of the activated faults, the authors concluded that the second main shock was probably due to unclamping by the first shock of a similarly oriented fault. This scenario could be proposed for either the NE or the NNW trending fault systems. However, an alternative scenario involving a more complex rupture with the quasi-simultaneous activation of both conjugate faults remains possible. Indeed, the events nucleated within the tectonic syntaxis between the Kirthar range and Sulaiman lobe, a kinematically unstable area.

In this paper, we present InSAR data in order to identify the fault segments activated during the seismic crisis. First, we perform a nonlinear inversion: One of the possible fault orientations for the first event can then be rejected. For the second event, two fault orientations remain possible. Linear inversion is performed for both scenarios to determine the slip distribution. Finally, the most likely rupture sequence is determined through stress-change modeling. Our preferred model involves conjugate faulting in the core of the tectonic syntaxis. We describe the whole earthquake sequence, the style of faulting, and the deformation distribution. Finally, these observations lead us to tectonic conclusions.

**Table 1.** Global Centroid Moment Tensor Data for the Studied Earthquakes<sup>a</sup>

Event	Date—Time (UTC)	Latitude (°N)	Longitude (°E)	M <sub>w</sub>	FP1 Strike/Dip/Slip	FP2 Strike/Dip/Slip
EQ1	28/10/08—22:33:12.9	30.47	67.43	5.3	<b>229/63/22</b>	128/70/151
EQ2	28/10/08—23:10:2.0	30.40	67.48	6.4	<b>304/73/171</b>	37/81/18
EQ3	29/10/08—11:32:48.6	30.29	67.57	6.4	324/68/−178	<b>233/88/−22</b>
EQ4	03/11/08—16:8:18.3	30.31	67.63	4.9	285/43/108	<b>82/50/74</b>
EQ5	15/11/08—15:21:11.5	30.31	67.56	4.8	28/78/−10	<b>120/80/−167</b>
EQ6	09/12/08—2:46:35.5	30.32	67.48	5.2	<b>64/79/7</b>	333/83/169
EQ7	09/12/08—5:53:45.8	30.31	67.5	5.3	<b>63/73/11</b>	330/80/163
EQ8	09/12/08—22:52:39.3	30.33	67.51	5.7	<b>62/75/0</b>	152/90/−165

<sup>a</sup>The most consistent nodal planes according to this study are in bold. Dates are formatted as day/month/year.

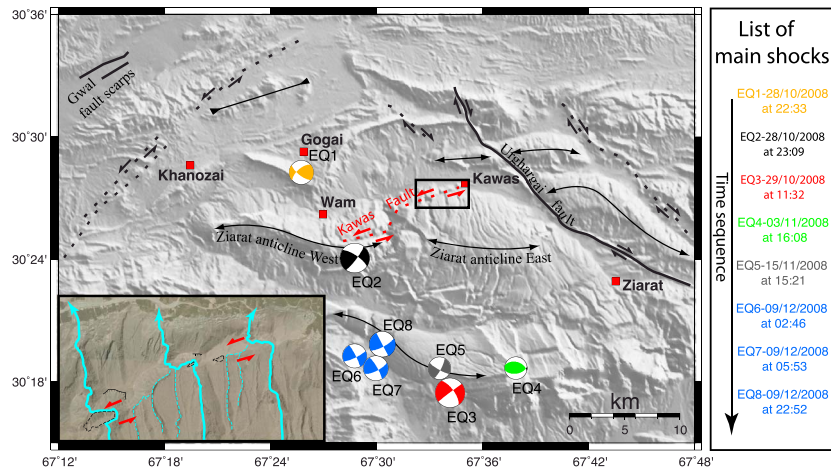


**Figure 2.** Location map for the Ziarat earthquakes according to the global CMT catalogue on a shaded DEM (SRTM3V3). Black continuous lines are mapped faults [Kazmi, 1979; Nakata et al., 1991]. Dashed lines are the strike-slip faults with the most evident morphology on the DEM and high-resolution imagery. Color image in inset corresponds to a detail of the Kawas fault strand on the high-resolution DigitalGlobe images available in Google Earth. The image frame is indicated by the black box on the map. We interpret bayonet shapes (i.e., dog-legs) along the mainstream channels as a result of the left-lateral motion on the fault. An additional normal component of motion is suspected. The hairpin loops of the stream channels along the fault may be related to diversion around landslide deposits (outlined by black dashed lines).

## 2. Measuring the Ground Displacement With InSAR: Method and Results

### 2.1. Interferometric Processing

We used C-band Envisat Advanced Synthetic Aperture Radar (ASAR) images (5.6 cm wavelength) and L-band Advanced Land Observing Satellite (ALOS) Phased Array Type L-band Synthetic Aperture Radar (PALSAR) images (23.6 cm wavelength) for our interferometric study. The ASAR images cover the epicentral area of the earthquakes and were acquired on the ascending path 213 and the descending path 363 (frames shown in Figure 1 and dates in Table 2). Incidence angles at scene centers are 40.9° for the ascending path and 22.8° for the descending path. The interferometric processing was carried out with CIAO software [Listner et al., 2010]. All differential interferograms with geometrical baselines smaller than 100 m were computed. The applied multilook to downsample the data is 4 pixels in range and 20 pixels in azimuth. The topographic fringes were removed based on the Shuttle Radar Topography Mission (SRTM) DEM (digital elevation model) [Farr et al., 2007]. For track 363, 5 images yielded 8 interferograms and for track 213, 12 images yielded 31 interferograms. The database of wrapped interferograms was filtered using the Multilink SAR method [Pinel-Puysségur et al., 2012], which enhances the wrapped phase signal quality based on interferogram network redundancy.

**Table 2.** SAR Image Acquisition Dates and Coseismic Pairs Used in This Study<sup>a</sup>

Envisat ASAR Path 363		Envisat ASAR Path 213		ALOS PALSAR Path 542	
Acquisition Dates	Coseismic Pairs	Acquisition Dates	Coseismic Pairs	Acquisition Dates	Coseismic Pairs
24/12/2005	24/12/2005-08/11/2008	17/04/2007	13/11/2007-17/03/2009	22/01/2007	22/01/2007-12/12/2008
04/03/2006	04/03/2006-08/11/2008	04/09/2007	06/05/2008-10/02/2009	12/12/2008	
17/06/2006	04/03/2006-13/12/2008	09/10/2007	09/10/2007-10/02/2009	27/01/2009	
08/11/2008		13/11/2007	06/05/2008-06/01/2009		
13/12/2008		06/05/2008	13/11/2007-06/01/2009		
		15/07/2008	09/10/2007-06/01/2009		
		19/08/2008			
		23/09/2008			
		02/12/2008			
		06/01/2009			
		10/02/2009			
		17/03/2009			

<sup>a</sup>Dates are formatted as day/month/year.

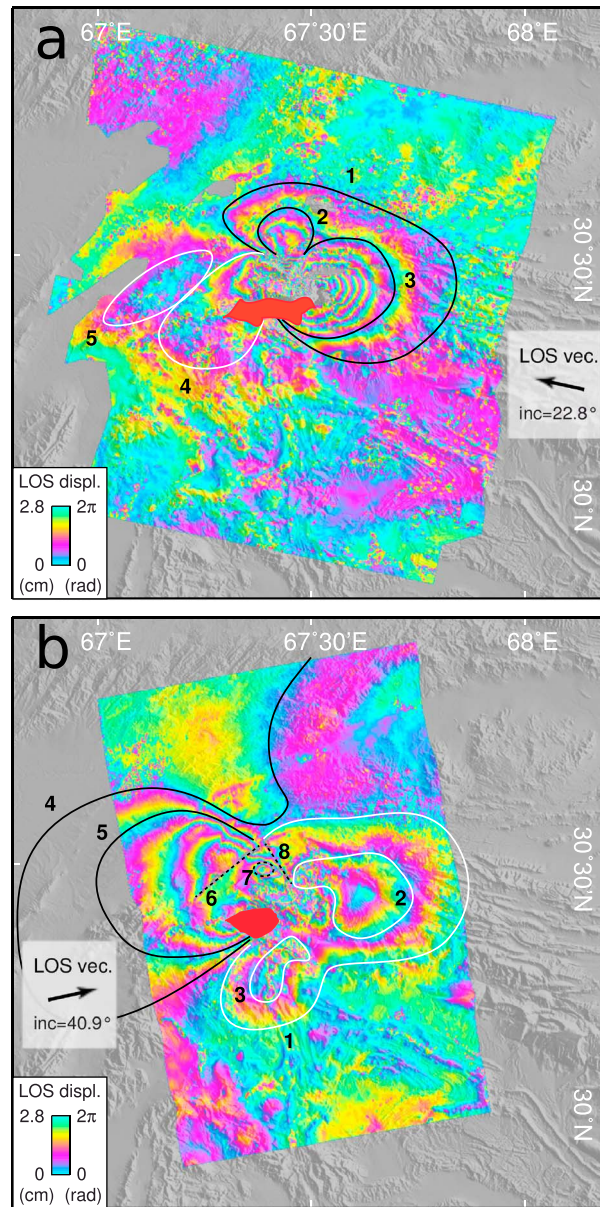


**Figure 3.** ASAR mean coseismic interferograms (rewrapped for better clarity). Areas that could not be unwrapped due to low coherence are masked. Positive line-of-sight (LOS) motion indicates displacement toward the satellite. The orientation of the LOS vector is shown by a black arrow. Positive lobes are shown in black and negative ones in white. (a) Descending average coseismic interferogram (mean of three interferograms), path 363. Two positive sublobes (2 and 3) appear inside a greater positive lobe (1). A negative lobe (4) and an additional negative area (5) are also delineated. (b) Ascending average coseismic interferogram (mean of six interferograms), path 213. Negative lobe 1 contains two sublobes (2 and 3) and is linked to negative area 4. Positive lobe 5 contains a sharp discontinuity (6) and attains its maximum in area 7. A linear discontinuity (8) is due to signal saturation. Decorrelated areas are masked in red.

The ALOS ascending interferogram (see Figure 4) covers the deformation zone only partly but gives complementary insight into the signal. Indeed, the fringe rate is saturated in some parts of the ASAR ascending interferogram whereas it is not saturated on the ALOS interferogram (for example, feature 8 on Figures 3b and 4).

Among the coseismic interferograms, some are affected by strong atmospheric effects due to at least one of the acquisition dates. The dates inducing strong atmospheric effects were determined using pairwise logic [Massonnet and Feigl, 1995]. For example, for track 213, we found that the tropospheric effects on 15 July 2008 strongly affected the radar wave propagation time as all interferograms using this date were affected whereas interferograms without this date were not affected [Pinel-Puysségur et al., 2012]. Similar analysis shows that significant atmospheric effects were also present on 19 August and 23 September 2008. We discarded the interferograms strongly affected by atmospheric effects.

The remaining coseismic interferograms were filtered using an adaptive filter [Goldstein and Werner, 1998]. After manually masking noisy areas, the interferograms were unwrapped with a weighted least squares algorithm [Ghiglia and Romero, 1994]. Six interferograms were unwrapped for path 213 and three interferograms for path 363 (see Table 2). Finally, the means of all unwrapped coseismic interferograms have been computed. They are shown in Figure 3 (phase rewrapped for better clarity). All the interferograms shown in this paper are geocoded. Postseismic interferograms have been computed as well for both ASAR paths (see Figure S1 in the supporting information).

The three L-band ALOS PALSAR images (see Table 2 and Figure 1) are taken from ascending path 542. The incidence angle at scene center is 38.7°. Three interferograms were computed with ENVI SARSCAPE software. Among them, only one coseismic interferogram is coherent due to its short perpendicular baseline of 202 m (22 January 2007 to 12 December 2008). It is shown in Figure 4. No further postprocessing was needed as it is very coherent.

### 2.2. Results and Challenges

The mean descending and ascending ASAR coseismic interferograms (see Figure 3) show that deformation spans 50 km in the east–west direction and 30 km in the north–south

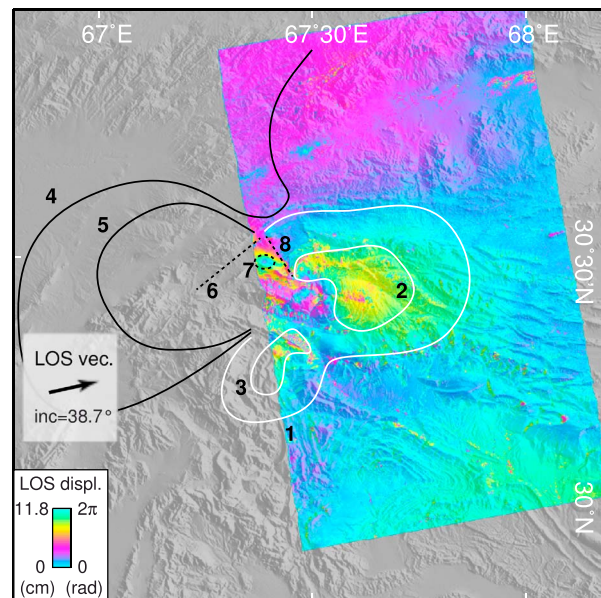


**Figure 4.** Ascending ALOS coseismic interferogram between 22 January 2007 and 12 December 2008, path 542. Delineated lobes are the same as in Figure 3b.

Postseismic interferograms (see Figure S1) show that minor postseismic deformation occurred in the area affected by the two main shocks. However, they also record the three shocks of 9 December 2008. Phase decorrelation and increased fringe rate indicate that these shocks induced deformation around  $30^{\circ}23'N$ ,  $67^{\circ}22'E$ , along the southwestern limb of the Ziarat fold. The decorrelation is likely due to saturation as the fringe rate is strong near the decorrelation zone. This suggests that the deformation was produced by slip on a shallow fault segment.

Despite the complementarity of all the ascending and descending C- and L-band interferograms, the determination of the fault rupture planes is challenging for several reasons. First, all coseismic interferograms integrate the deformation due to many events: the two  $M_w = 6.4$  main shocks, the  $M_w = 5.3$  foreshock, and several  $M_w > 4.0$  aftershocks. Given their shallow depths

and focal mechanisms, they all might have contributed to deformation measurable by InSAR (Tables 1 and 2). As the deformations due to all these earthquakes are combined and since the earthquakes occurred close to each other, their respective contributions cannot be easily separated.

Second, the absolute locations of these seismic events are not well constrained. Indeed, absolute location using global seismic networks suffers from large uncertainty. As an example, the distance between the preliminary earthquakes locations used for early static stress variations estimates [McCloskey and Nalbant, 2009] and the regions affected by large line-of-sight (LOS) changes is larger than 20 km. The latest relocations provided by USGS, global centroid moment tensor (CMT), or ISC better match the interferograms but still appear shifted by several kilometers.

Moreover, the traces of the activated faults are unknown. Indeed, none of the active fault segments mapped in the area [Kazmi, 1979; Nakata et al., 1991] lies in the region affected by the largest deformation. Furthermore, the geological survey of local surface effects detected fresh ground cracks and fissures in the epicentral region but no surface ruptures were clearly identified [PMD report, 2009]. Nevertheless, high-resolution optical imagery and DEMs reveal lateral offset and beheaded streams along a 12 km long surface fault trace striking  $N60-75^{\circ}$  that dislocates the Ziarat anticline (see Kawas fault in Figure 2 and optical image in the inset). The lateral offset is particularly visible on a 5 km segment near the eastern termination of the Kawas fault (Figure 2). This fault is located less than 5 km from the decorrelated area in the InSAR data and likely extends through it. This suggests that this sinistral strike-slip fault could be the source of one of the earthquakes. However, there are few complementary neotectonic clues revealing the Holocene or even Quaternary activity of strike-slip and thrust faults in the vicinity.

Another issue prevents precise location of the seismic events based on the InSAR data. Decimetric coseismic slip often leads to deformation saturating C-band interferograms near the fault, thus indicating possible fault locations. In our interferograms, one area is decorrelated (Figure 3). However, the DEMs and high-resolution imagery of this area do not reveal any geomorphic evidence of fault segment activity. Instead, this decorrelation is probably due to landsliding or major surface change and not to saturation. The ALOS interferogram does not suggest any trace of a surface rupture either. Moreover, disparity maps from subpixel correlation have been computed on both ASAR tracks but did not show any significant signal. Consequently, the modeling and interpretation of these interferograms are a challenging problem.

**Table 3.** Results of the Nonlinear and Linear Inversions for the Four Tested Scenarios for Envisat Tracks 213 and 363

	Data		RMS of the Nonlinear Inversion Residuals (cm)				RMS of the Linear Inversion Residuals (cm)			
	RMS (cm)	Samples	A	B	C	D	A	B	C	D
Track 213	3.46	403	1.43	1.53	1.81	1.80	1.07	1.14	1.59	1.50
Track 363	4.16	436	1.46	1.61	1.86	2.46	1.19	1.16	1.52	1.72

<sup>a</sup>The RMS values and number of samples of the downsampled data vectors are given in the second and third columns. The four following columns show RMS residuals of the nonlinear inversion for each scenario (A to D, see section 3.3) and the four last columns for the linear inversion (see section 3.4 for more details).

### 3. Displacement Inversion

#### 3.1. Modeling Strategy

At least two distinct sources must be accounted for to model the InSAR data. These sources correspond to the two  $M_w = 6.4$  main shocks of 28 October 2008, 23:10 (EQ2) and 29 October 2008, 11:32 (EQ3). Other events within the 2008 seismic crisis could have also contributed to the observed deformation despite their lower seismic moment. If they are not taken into consideration, these smaller events may bias the estimation of the deformation produced by the two main shocks. However, for the sake of simplicity, we assume that modeling the two main shocks is sufficient to interpret the first-order features of the InSAR data. In other words, we assume that smaller earthquakes' deformation is negligible enough compared to the two main shocks' deformation to allow for a reliable estimation of the source parameters of the two main shocks. The validity of this assumption will be assessed a posteriori by examining the residual LOS displacement maps and by comparing the seismic moment of the two modeled earthquakes with the actual value deduced from seismology.

According to the global CMT, the two main shocks EQ2 and EQ3 have similar strike-slip mechanisms with  $P$  axes oriented N-S and  $T$  axes oriented E-W. However, given the magnitude of the earthquakes and despite the local seismological data [Lisa and Jan, 2010], it is difficult to determine which focal plane is associated with each earthquake. To answer this question, we perform a series of inversions on the InSAR data set.

Each source might be either right lateral with a NW-SE strike or left lateral with a NE-SW strike. Thus, four scenarios defining the relative locations of the two sources are possible. Scenario A involves a NW-SE right-lateral fault for EQ2 and a NE-SW left-lateral fault for EQ3. Scenario B involves two NW-SE right-lateral faults for both EQ2 and EQ3. Scenario C involves two NE-SW left-lateral faults for both EQ2 and EQ3. At last, scenario D involves a NE-SW left-lateral fault for EQ2 and a NW-SE right-lateral fault for EQ3. As shown below, while InSAR observations clearly exclude scenarios C and D, they are unable to favor either A or B as a "best fitting" scenario. Nevertheless, stress-change modeling allows us to infer a most likely scenario, assuming that static stress triggering is a plausible mechanism explaining the sequence of two events.

#### 3.2. Data Preprocessing

To keep the problem computationally tractable, the Envisat ASAR ascending and descending interferograms (tracks 213 and 363, respectively) are subsampled at a density depending on distance from the assumed earthquake source location, as in Grandin *et al.* [2009]. The size of the original InSAR pixels is 90 m. Here using the coordinates 67.45°W, 30.45°N as the origin, we subsample the data using grid spacings of 2.2 km, 4.4 km, and 8.8 km for the distance ranges 0–15 km, 15–30 km, and 30–300 km, respectively. The number of samples and the root-mean-square (RMS) value of the subsampled data vectors are listed in Table 3.

The ALOS coseismic interferogram is not used to constrain the inversion as the C-band data alone seem to be sufficient for a simple analysis of this complex signal. Moreover, the ascending Envisat and ALOS acquisitions were performed with nearly equal look vectors. Finally, the ALOS coseismic interferogram only covers the eastern half of the area affected by significant deformation. In fact, we compared the deformation measured by ALOS and by Envisat ascending data over their common area and it appeared that the deformation signal was very similar in both cases. This agreement indicates that the processing of Envisat data, in particular, the tricky unwrapping step, was correct over this common frame.

#### 3.3. Nonlinear Inversion of Fault Geometry

We first test simple models involving uniform slip on rectangular fault planes [Okada, 1985]. The inversion is performed using the nonlinear inversion method of Tarantola and Valette [1982]. Starting from an a priori

**Table 4.** Source Parameters From Variable-Slip Inversion (Scenarios A to D)

Scenario	Event	Longitude (°N)	Latitude (°E)	Depth (km)	Strike (°N)	Dip (Degree)	Rake (Degree)	Moment ( $\times 10^{18}$ N m)	$M_w$
A	EQ 2	67.4177	30.5078	7.6	312.3	73	174	6.00	6.4
	EQ 3	67.4471	30.4041	7.9	236.2	89	-6	5.89	6.4
B	EQ 2	67.4402	30.4876	7.8	314.9	78	179	7.29	6.5
	EQ 3	67.4435	30.3876	8.0	330.2	81	169	6.24	6.5
C	EQ 2	67.4160	30.4738	7.1	30.9	76	11	3.59	6.3
	EQ 3	67.4503	30.4035	8.2	48.7	80	8	5.50	6.4
D	EQ 2	67.3976	30.5017	7.5	39.2	60	26	2.55	6.2
	EQ 3	67.4500	30.4483	8.8	325.2	79	-179	6.64	6.5

configuration, the inversion determines the best fault location (latitude, longitude, and depth), fault geometry (length, dip, and strike), and slip vector (rake angle and slip magnitude). All a priori parameters of fault location and moment tensor are set according to the global CMT solution. The only exception is the centroid depth, as the value provided by the global CMT (12 km) is too deep to explain the amplitude of the deformation observed by InSAR. Therefore, we start with an a priori value of 3.5 km for the depth of the top edge of the fault. Fault width is held fixed as this particular parameter was found to be nearly impossible to constrain solely from InSAR data, due to a trade-off with slip magnitude. The width is fixed at 6 km; thus, the depth of the fault's downdip end is around 8–9 km. It is consistent with the locking depth for the fault that produced the nearby 1931 Mach earthquake [Szeliga *et al.*, 2009]. The a priori fault length is set to 10 km.

The RMS values of the residual vectors for each scenario on tracks 213 and 363 are listed in Table 3. These preliminary inversions indicate that the data are best explained by scenario A, in which the earthquakes are associated with two conjugate faults, rather than two subparallel faults. In the best scenario (A), one of the fault planes, presumably associated with EQ2, has a NW-SE strike, whereas the second fault plane, likely related to EQ3, is located farther to the south, on a NE-SW trending structure. However, the superiority of scenario A compared to scenario B in terms of fit to the data is not sufficiently strong to dismiss scenario B. One can nevertheless exclude the occurrence of EQ2 on a fault trending NE-SW, hence discarding scenarios C and D. Indeed, residuals in the northern part of the area of significant deformation clearly indicate that the causative fault in this specific area is striking NW-SE.

### 3.4. Linear Inversion of Slip Distribution

In the second step, for each of the four scenarios, we determine the slip distribution of both earthquakes, on two discretized fault planes with fixed geometry. Solving for variable slip allows us to reproduce second-order features of the data set that cannot be fit with the simple, uniform slip model. Details of the inversion procedure are described in Jónsson *et al.* [2002] and Grandin *et al.* [2009]. Fault planes determined from the nonlinear inversion step are extended so that their along-strike length is set to 30 km and their along-dip width to 15 km. The planes are then discretized into  $20 \times 10$  grids of square elements. The distribution of slip vectors is determined by a linear least squares inversion. Smoothing constraints are included via a Tichonov regularization using the second-order spatial derivative of slip. The stringency of the smoothing constraint is adjusted through an  $L$ -curve analysis of the roughness of the slip solution against misfit to the data. Using a non-negativity constraint, slip vectors are forced to be within  $90^\circ$  of the a priori direction given by the rake angle deduced from the nonlinear inversion step. Slip is assumed to taper to zero along the vertical sides and at the bottom of the fault plane. For each interferogram, orbital errors are modeled as a first-order polynomial surface, while stratified tropospheric delays are mitigated by modeling a linear relation between phase and elevation.

The RMS of the residual vectors for each scenario on tracks 213 and 363 are listed in Table 3 and the source parameters in Table 4. The best fitting slip distributions for each scenario confirm that scenarios A and B are more successful than scenarios C and D at explaining the data. However, the apparent superiority of scenario A compared to scenario B that was previously inferred from the nonlinear inversion appears to vanish (see Figures 5 and 6 and Table 3): While scenario A best explains the ascending interferogram

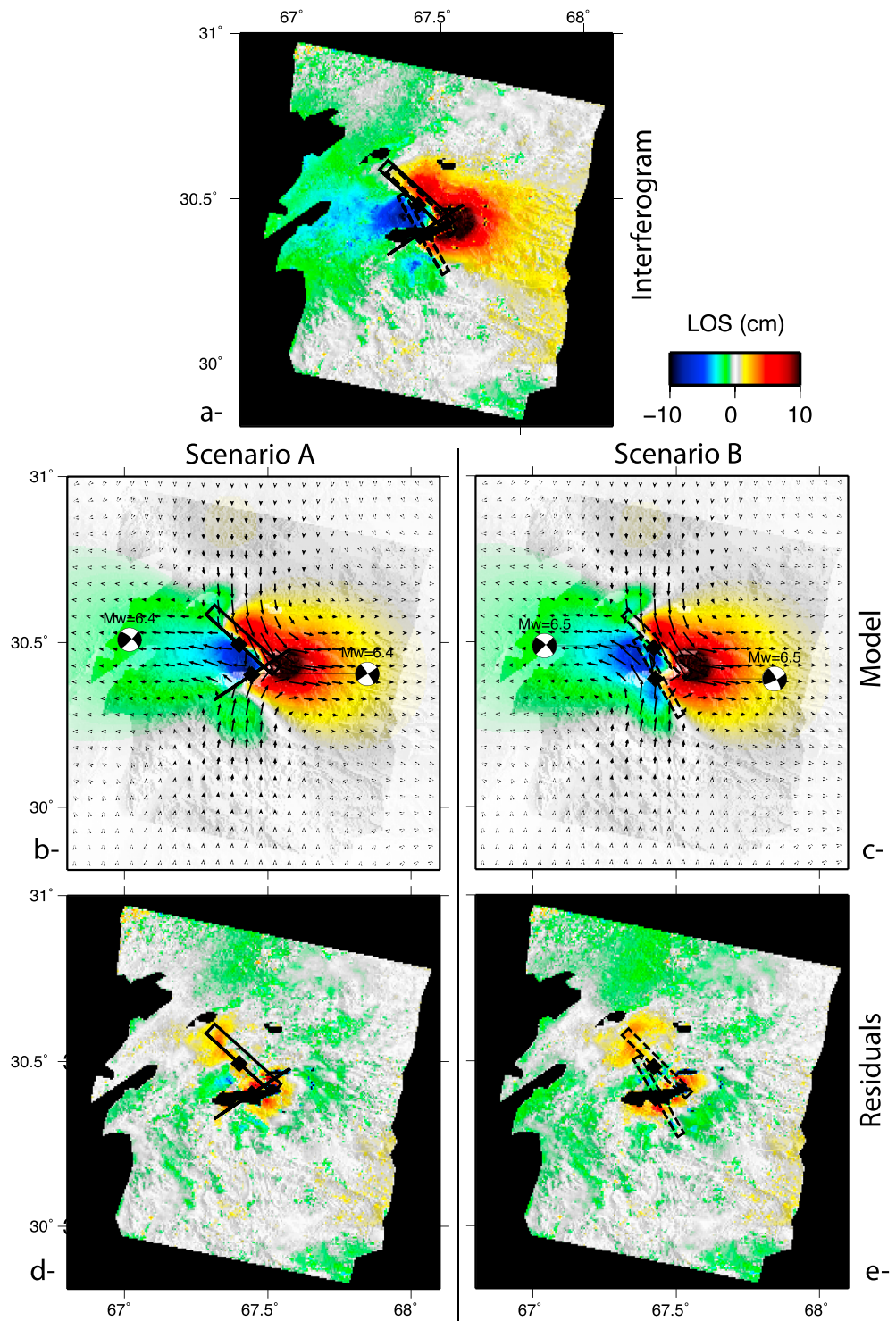


**Figure 5.** (a) Descending track coseismic ASAR unwrapped interferogram. (b and c) Synthetic interferograms for two variable-slip conjugate faults (scenario A) and NW-SE striking planes (scenario B). (d and e) Residuals of model scenarios A and B.

(Figure 6), scenario B is slightly better at fitting the descending interferogram (Figure 5). Although a more complex slip distribution better models the fringe pattern than a simple uniform slip model does, such an approach does not relieve the inherent ambiguity between the two focal planes involved in earthquake 2. Figure 7 shows the inverted slip distribution on F1 and F2 for scenarios A and B. For scenario

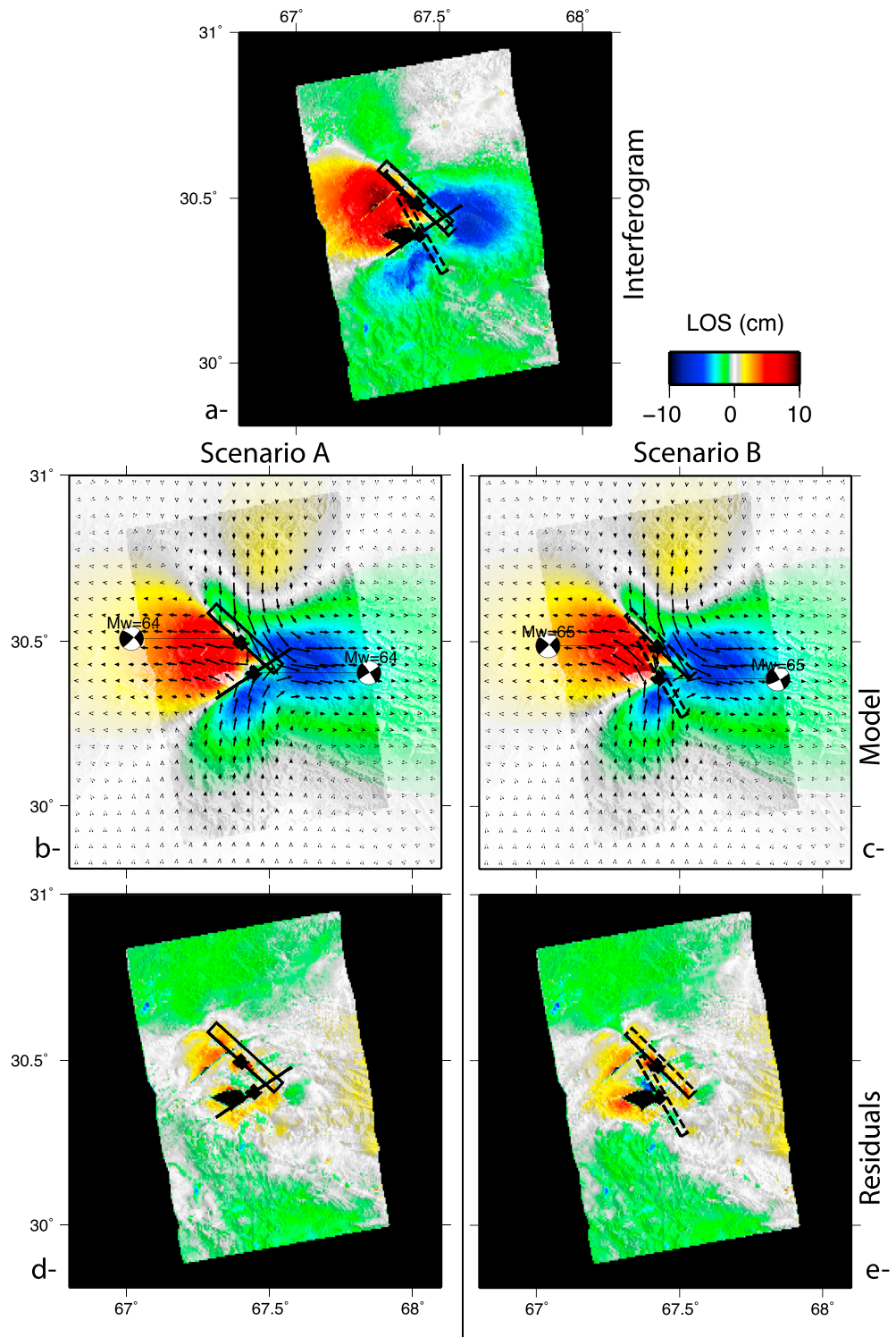


**Figure 6.** (a) Ascending track coseismic ASAR unwrapped interferogram. (b and c) Synthetic interferograms for two distributed slip conjugate faults (scenario A) and NW-SE striking planes (scenario B). (d and e) Residuals of model scenarios A and B.

A, the a priori faults F1 and F2 on which the linear inversion is performed cross, which would be physically inconsistent. However, the fault slip on F1 is restricted to the area northwest of the junction with F2. Indeed, the deformation southeast of this junction is negligible, meaning that F1 does not cross but only abuts F2. Thus, scenario A is plausible, as well as scenario B.

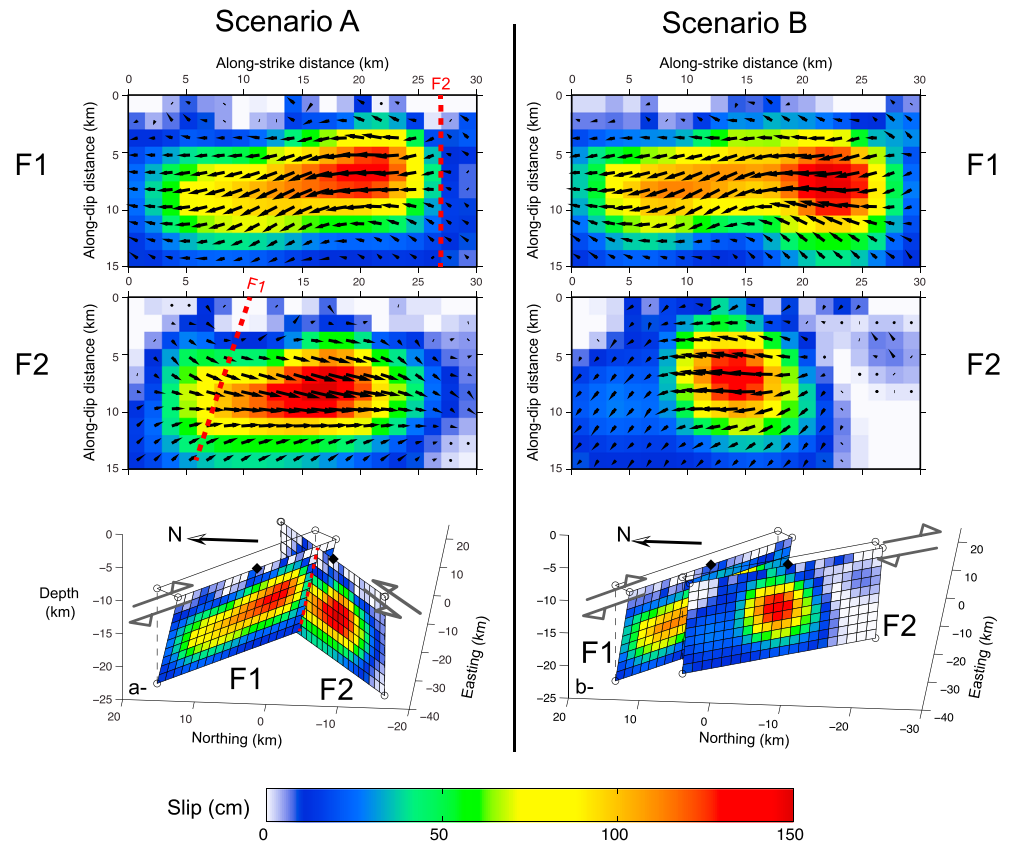


**Figure 7.** Distribution of slip on the fault planes of earthquakes 2 (F1) and 3 (F2) for (a) scenario A, the best model with two conjugate faults, and (b) scenario B, the best model with two NW-SE sources. For scenario A, the red dashed lines represent the intersection of F1 and F2. It can be noted that the inverted slip on F1 southeast of F2 is negligible; this is physically realistic as it means that F1 does not cross F2.

#### 4. Determination of the Best Scenario by Stress-Change Modeling

The static stress change induced by an earthquake can promote or delay the occurrence of seismic slip on a neighboring fault depending on the focal mechanisms and the relative configuration of the two events [e.g., King *et al.*, 1994]. To determine the most likely scenario for the 2008 sequence, we use the slip distributions obtained from the linear inversion (Figure 7) to compute the stress change induced by EQ2 resolved on the fault plane of EQ3. Slip is promoted on the receiver fault plane if the normal stress change decreases (i.e., in case of an unclamping) and/or if the shear stress component oriented in the same sense as the slip vector increases. Conversely, slip is impeded in case of a clamping of the fault plane and/or if the shear stress change tends to oppose the slip tendency favored by the regional stress conditions. The combined effect of normal stress change  $\Delta\sigma_n$  (positive for extension) and shear stress changes  $\Delta\tau_s$  is captured by the sign of the Coulomb stress change defined as

$$\Delta CFS = \Delta\tau_s + \mu \times \Delta\sigma_n \quad (1)$$

where  $\mu$  is the effective friction coefficient. We took an intermediate value  $\mu = 0.4$  as we had no prior knowledge of the effective friction coefficient in this region, the span of plausible values lying between 0 and 0.75 [King *et al.*, 1994].

In order to determine the most likely rupture scenario, we compute the Coulomb stress change on the fault plane corresponding to EQ3 in response to slip on the fault plane of EQ2, using analytic solutions provided by Okada [1992]. Since scenarios C and D have been excluded by the above analysis, only scenarios A and B are tested here. The primary difference between the two latter scenarios lies in the orientation of fault 2 relative to fault 1, with fault 1 remaining fixed. Therefore, the main mechanism leading to Coulomb stress transfer from EQ2 to EQ3 will differ significantly from one scenario to the other. In scenario A, the two faults

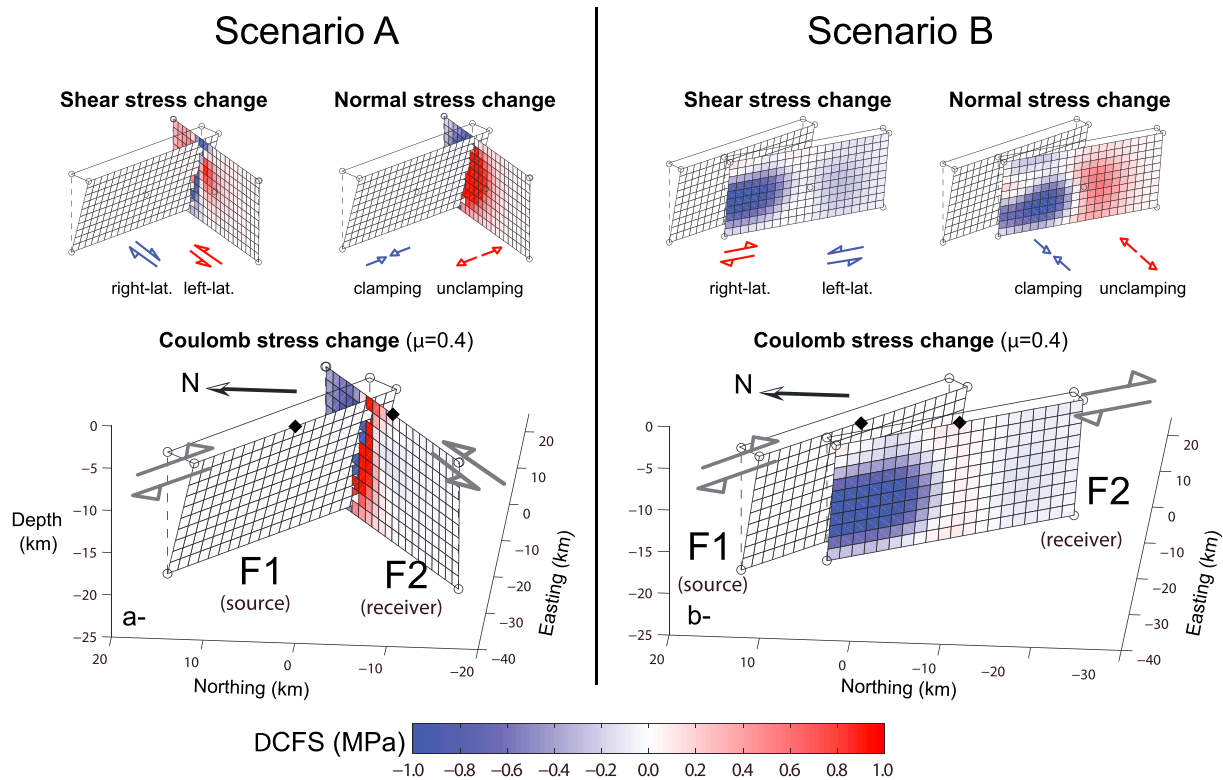


**Figure 8.** Coulomb stress changes on the fault plane corresponding to EQ3 (F2) in response to slip on the fault plane of EQ2 (F1) for (scenario A) the best model with two conjugate faults and (scenario B) the best model with two NW-SE sources. (top row) Shear stress and normal stress changes and (bottom row) the total Coulomb stress change.

are conjugate, with the fault plane of EQ2 being right lateral, oriented perpendicularly to, and abutting the left-lateral fault plane of EQ3. In this scenario, the normal stress change on the receiver fault constitutes the main contribution to the Coulomb stress change. Conversely, in scenario B, the faults both slip with a right-lateral sense of motion and are almost parallel to each other. Therefore, Coulomb stress change is essentially determined by the shear stress change.

In scenario A (Figure 8a), we observe a large normal stress reduction (unclamping) in excess of 1 MPa in the area of significant slip on fault 2 in response to slip on fault 1, i.e., to the SW of the intersection between the two faults (Figure 7). Shear stress changes oscillate from positive (right-lateral slip is promoted) to negative (left-lateral slip is promoted) near the intersection of the two fault planes, albeit with a smaller magnitude than normal stress change. As mentioned in *Woessner et al.* [2012], when the causative fault is close to the receiver fault, the sign of the Coulomb stress change is uncertain, especially when the values of the Coulomb stress change are close to 0. Thus, the sign of the shear stress change should be regarded with caution. However, in this case, the normal stress component dominates the shear stress component and the unclamping (clamping) of the southwestern (northeastern) part of F2 is a first-order feature. Hence, the net response of fault 2 is an increase of slip tendency southwest of the contact between the two fault planes, for nearly any direction of slip of the receiver fault.

In scenario B (Figure 8b), moderate unclamping of fault 2 occurs only along the southern half of the fault plane (<0.6 MPa), while the northern half of the fault plane experiences significant clamping (>1 MPa). Regarding the shear stress tendency, calculations show that left-lateral slip is strongly promoted (up to more than 2 MPa), while right-lateral slip is nowhere favored. As the sign of the shear stress remains constant, this tendency can reasonably be considered as a first-order feature. This is because the two faults are nearly parallel to each other, so that slip on one of these faults efficiently relieves any tectonically induced stress on its companion. In this case, due to the geometric configuration, the shear stress component dominates the normal component. Consequently, the Coulomb stress change does not favor the occurrence of right-lateral slip on fault 2 in response to right-lateral slip on fault 1. As we already know that in scenario B,

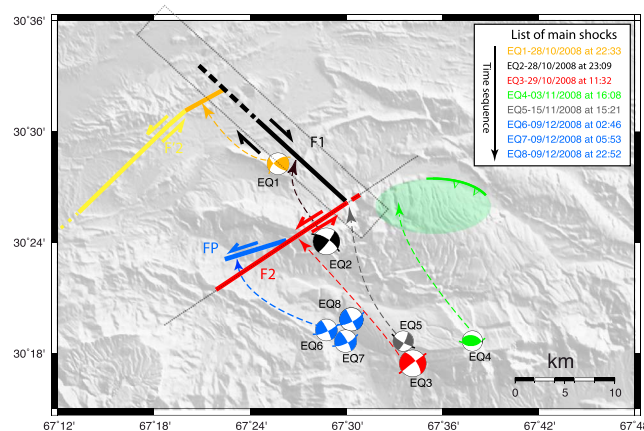


**Figure 9.** Cartoon illustrating the structures activated during the seismic crisis as well as their time sequence of activation according to our preferred model (color coded). The dotted line and rectangle correspond to the locations of the fault planes in the best model with two conjugate faults. Shaded DEM from SRTM3V3. Focal mechanisms from the global CMT catalogue. Tick marks on the focal mechanisms indicate the fault plane solutions deduced from this study. Dashed arrows link the CMTs to the seismogenic structures. Note the systematic 10–15 km SE shift between the CMTs and the structures, revealing a seismic location bias.

slip on fault 2 should be right lateral, we consider scenario B to be unlikely. On the contrary, there is no reason to discard scenario A. We conclude that, on a mechanical basis, scenario A is more likely than scenario B.

Note that this conclusion involves several caveats. The interferogram stacks, even after the various processing steps, contain some residual errors. The nonlinear analysis includes only two segments, while in reality other minor faults were activated as well, as explained in section 5.2. This may have influenced the outcome of the uniform fault model, thereby also affecting the distributed slip results, and finally the stress analysis as well. The stress analysis depends on the value of the effective friction coefficient and on the inferred slip distribution. Thus, we cannot definitively discard scenario B nor promote scenario A. In fact, the observed deformation may be

a combination of both scenarios as their LOS projections are very similar. This alternative scenario may be possible if some slip occurred on the NW-SE fault 2 of scenario B after the slipping of the NE-SW fault 2 of scenario A. However, it is even more difficult to demonstrate that such a scenario occurred.

In fact, scenario A is consistent with other observations. Indeed, in this scenario, fault 2 lies along strike from the fault activated during the 9 December 2013 events (see Figure S1). Moreover, it also lies along strike from the Kawas fault dog-legs shown in Figure 2. From now on, we therefore assume that scenario A occurred, i.e., that fault 2 is a left-lateral NE-SW fault. We draw our conclusions from this assumption.

## 5. Discussion

### 5.1. Seismological Aspects

Contrarily to what has been deduced from preliminary studies [e.g., McCloskey and Nalbant, 2009; Lisa and Jan, 2010; Yadav et al., 2012], neither the active faults of the NE trending Quetta line surveyed by Nakata et al. [1991] (i.e., Pishin, Gwal, Churmian, and Balozai active faults) nor the SE trending Urghargai fault described by Kazmi [1979] was activated during the 2008 Ziarat earthquake sequence. Instead, our preferred model of the deformation field measured from InSAR demonstrates that coseismic slip during the seismic crisis was mainly accommodated on two nearly conjugate structures: (1) a WNW directed dextral strike-slip fault and most probably (2) an ENE directed sinistral strike-slip fault. According to our preferred model (scenario A), these faults accommodated similar amounts of average slip. Assuming typical values for density and shear wave velocity, respectively, 2900 kg/m<sup>3</sup> and 3.5 km/s, these ruptures correspond to seismic moments equivalent to  $M_w = 6.5$  and 6.4. These values are almost identical to the magnitudes of the events deduced from seismological observations ( $M_w = 6.4$ ), thereby demonstrating that the postseismic slip on the structures activated during the two main shocks was probably very limited. In any case, postseismic deformation following the 2008 Ziarat sequence was much smaller than the  $56 \pm 19\%$  postseismic slip observed after 2005 Muzaffarabad earthquake, which occurred within the nearby NW Himalayan syntaxis [Jouanne et al., 2011].

We ran forward models to simulate the three 9 December 2008 events (EQ6, EQ7, and EQ8). We found that a rupture with ~70 cm slip accommodated on a  $5 \times 5$  km patch reproduces the signal well (see FP in Figure 9), equivalent to a  $M_w = 5.8$  earthquake. This estimate is consistent with the seismic moment released during the three  $M_w > 5$  events that occurred on 9 December 2008, which corresponds to a total seismic moment release equivalent to  $M_w = 5.8$ .

**Table 5.** List of Earthquake Doublets on Conjugate Strike-Slip Faults

Name	Year	Mw Event 1	Mw Event 2	Relative Strike Angle and References	Delay (Days)	Tectonic Context
Superstition Hills	1987	6.2	6.6	90° [Larsen <i>et al.</i> , 1992]	0.5	Transform plate boundary
Al Hoceima	1994–2004	6.0	6.4	70° [Akoglu <i>et al.</i> , 2006] to 90° [Biggs <i>et al.</i> , 2006]	3561	Oblique convergence
Kagoshima	1997	6.1	6.0 <sup>b</sup>	90° [Toda and Stein, 2003]	48	Arc-related extension
Ziarat	2008	6.4	6.4	76° <sup>a</sup>	0.5	Syntaxis
South Rigan	2010–2011	6.5	6.2	82° [Walker <i>et al.</i> , 2013]	38	Diffuse shearing
Gulf of Alaska	1987	7.2	7.8 <sup>c</sup>	85°–105° [Hwang and Kanamori, 1992]	13	Oceanic intraplate
Wharton Basin	2000	7.8	7.4	90° [Robinson <i>et al.</i> , 2001]	1.7E-4 (15 s)	Diffuse oceanic boundary
Eastern Indian Ocean	2012	8.6	8.2 <sup>d</sup>	90° [Meng <i>et al.</i> , 2012]	8.3E-2 (2 h)	Diffuse oceanic boundary

<sup>a</sup>This study.

<sup>b</sup>The second main shock itself consisted of a complex rupture occurring on two conjugate strike-slip faults.

<sup>c</sup>The sequence consisted of three main shocks: One E-W oriented left-lateral earthquake followed by two N-S oriented right-lateral events. Here only the first and second main shocks are considered. The third main shock, with  $M_w = 7.7$ , occurred 97 days after the second main shock, along the southern continuation of the structure involved in the second main shock.

<sup>d</sup>The first main shock of the 2012 Eastern Indian Ocean sequence features a complex succession of subevents occurring within a few minutes on a set of at least three mutually perpendicular strike-slip faults. Here these subevents are collectively treated as a single event. The second main shock refers to an earthquake that occurred 2 h later on a structure oriented perpendicularly to and abutting the terminal segment of the first main shock (see Meng *et al.* [2012] for details).

## 5.2. Kinematic Interpretation

In this study, we attribute respectively the ruptures of the abutting WNW and ENE trending faults F1 and F2 to the 28 October 2008 23:09 and 29 October 2008 11:32 seismic events (Figure 9). The first earthquake most likely triggered the second by almost pure unclamping, given its geometry. This scenario would fit with the behavior previously observed during several past seismic sequences involving two (or more) main shocks on conjugate strike-slip faults (Table 5).

However, some features in the interferograms are not satisfactorily explained by our “best” scenario (Figures 5d and 6d). The most conspicuous residual feature is a 15 to 20 km long sharp and straight signal visible on the ASAR ascending interferogram (noted 6 in Figure 3b). As this signal is well localized, the fault trace can be deduced from phase discontinuity on the interferograms (about one fringe). This discontinuity follows a northeast striking segment. This feature can be explained by a shallow left-lateral strike-slip fault (F’2 in Figure 9). This feature is visible in the topography and is shown in Figure 2, north and west of Khanozai. It is probably an older structure that has been reactivated. We ran forward models to simulate this residual fringe pattern and found that left-lateral slip of 3.5 cm on a vertical strike-slip fault accurately reproduces the measured deformation. The measured azimuth on the inferred fault segment is N226°E, which would be consistent with the occurrence of EQ1 on FP1 (N229°E; see Table 1). However, the length of the activated fault segment (15–20 km) and the magnitude of slip on this segment (<5 cm) do not fit commonly observed scaling relationships between earthquake source parameters. Indeed, in order to satisfy the seismic moment magnitude of 5.3, the fault segment has to slip between the surface and a depth of ~2–3 km, which yields an implausible fault aspect ratio of 1:10. Therefore, although EQ1 likely contributed to the residual pattern on F’2, the actual origin of this deformation remains to be understood. Induced slip triggered by the two main shocks [Fialko *et al.*, 2002] may be an alternative source of deformation, though the two are not mutually exclusive. F’2 might be a coseismic break as well as a postseismic break.

Another discontinuity remains unexplained by the model. It is a 10 km long linear feature, clearly visible on the ALOS interferogram (feature 8 in Figure 4) and saturated on ASAR ascending interferograms (feature 8 in Figure 3b). However, it is hardly visible on the descending interferograms. Pure strike-slip motion with this azimuth would project much better on the descending than on the ascending LOS, which is the opposite of what we observe. Even if the motion was a combination of vertical and horizontal components, it would be unlikely that it occurred on the vertical plane that follows the trace of the discontinuity. This observation suggests localized northeast–southwest extension. We interpret this area as being affected by tension cracks (Figure 10). Although we did not model this extension, we measured the phase jump across the discontinuity on ALOS and ASAR ascending interferograms. Assuming that the deformation is mainly horizontal and normal to the discontinuity, we found that the extension increases from north to south, up to a maximum of about 10 cm at its southern tip.

Furthermore, the interferograms covering the 9 December 2008 events indicate that earthquakes EQ6–7–8 are associated with FP (Figures 9 and S1). Therefore, when compared to the actual maximum deformation

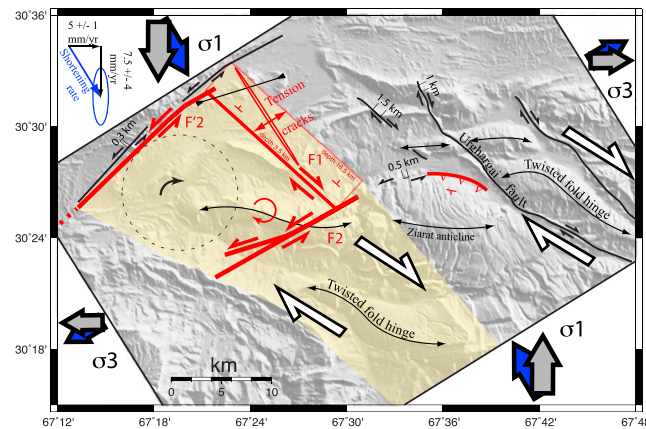


**Figure 10.** Structural and kinematic interpretation of the local tectonic structures according to our preferred model. Red lines are fault segments and a zone of fractures activated during the 2008 seismic crisis as revealed by this study. Piercing points and numbers along the fault traces indicate some offsets (in kilometers) along the major faults. The yellow band associated with the large white arrows corresponds to a dextral shear zone affecting the tectonic syntaxis. Red and black curved arrows indicate the block rotation between F1 and F2. The maximum principal stress  $\sigma_1$  probably falls between the azimuth of shortening (blue arrows) and the  $P$  axis of the local focal mechanisms (grey arrows).

location deduced from InSAR, the hypocentral locations of EQ1-2-3 and EQ6-7-8 determined by the global CMT/ National Earthquake Information Center appear systematically shifted southeast of the activated faults (Figure 9). The shift is about 15 km. EQ4 (3 November 2008) and EQ5 (15 November 2008) are probably similarly mislocated. The former, which is the only earthquake in the sequence with a reverse faulting mechanism, could be associated with the décollement under the main Ziarat anticline. The latter may correspond to the eastern tips of faults F1 or F2. This result seems reasonable because both fault plane solutions are consistent with motion on these respective faults.

### 5.3. Implication for Regional Tectonics

Overall, our study documents a complex earthquake sequence in a region where neotectonic constraints are scarce. Further understanding of this event within the

regional tectonic framework remains challenging, given the limited knowledge of the interseismic kinematics of this area. However, the only velocity field measurement in the region does incorporate a campaign GPS profile measured across the Chaman and Gazaband faults at the latitude of Ziarat (see Figure 1 for locations). These data allowed *Szeliga et al.* [2009] to propose  $5 \pm 1$  mm/yr of E-W shortening, a value similar to the 3.5 and 7.5 mm/yr respectively proposed by *Bernard et al.* [2000] for E-W and N-S convergence components relative to India.

This NW-SE convergence velocity relative to the Indian plate is consistent with the north-south to NNW-SSE maximum principal stress  $\sigma_1$ , as deduced from the focal mechanisms within 30 km, and appears perpendicular to an E-W to NE-SW oriented minimum principal stress  $\sigma_3$  (Figure 10).

The simplest way to interpret the 2008 seismic sequence fault patterns is with a pure shear Anderson-Coulomb model. Indeed, several characteristics are typical of a pure shear model: (a) the two almost-conjugate dextral and sinistral strike-slip faults broke quasi-simultaneously; (b) they accommodated similar amounts of slip, inducing the meter-scale extrusion of an  $\sim 50$  km<sup>2</sup> and  $\sim 10$  km thick block between F1 and F2 in the direction of the minimum principal stress,  $\sigma_3$  (Figures 9 and 10); and (c) these faults are short, hardly expressed at the surface and thus cannot be clearly associated to major structures of the neighboring area. Furthermore, (d) the orientation of the maximum principal stress,  $\sigma_1$ , makes an angle of about  $30^\circ$  with the dextral strike-slip F1, (e) the extension fractures detected north of F1 (Figure 10) are collinear to  $\sigma_1$  and perpendicular to  $\sigma_3$ , the extension axis [e.g., *Cloos*, 1955], and (f) similarly, the most prominent folds and thrusts appear to be oriented almost perpendicularly to the shortening axis (Figure 10).

However, this simplistic model does not explain some observations. Indeed, the angle between fault F2 and the direction of shortening is around  $50$ – $70^\circ$  (Figure 10). Although this angle can increase above  $60^\circ$  in laboratory experiments, the two angles between fault strikes and the direction of shortening remain equal to each other in pure shear models. Furthermore, pure shear models predict an angle between the two faults of  $50^\circ$  to  $60^\circ$ , whereas a nearly perpendicular angle is actually observed. Perpendicular conjugate faults are also commonly observed in many other strike-slip environments [e.g., *Sylvester*, 1988; *Thatcher and Hill*, 1991]. The coeval rupture of the two mutually perpendicular fault orientations during the 2008 Ziarat earthquake sequence (as well as other sequences elsewhere; see Table 5) clearly points to contemporaneous activity of the two fault families. Indeed, whatever the scenario, A (our preferred scenario) or B or a combination of both, some deformation was indisputably accommodated on both NE-SW and NW-SE fault systems as (1) one main shock at least was accommodated on a NW-SE fault (2) and at least two NW-SE faults, F'2 and FP, were activated during the earthquake sequence.

These two observations could be partially reconciled within a simple shear model involving a large N130° right-lateral strike-slip (wrench) fault system [Sylvester, 1988] crossing the western part of the Ziarat fold (Figure 10). Indeed, the Ziarat anticline western termination has a twisted hinge suggesting significant external clockwise rotation, whereas the pure shear model does not produce rotation (see Figures 2 and 10, Ziarat anticline west). Although less significant than the westward escape of the block between F1 and F2, such a rotation occurs right in the twisted segment of the Ziarat fold hinge. Indeed, the net left-lateral slip along F2 and FP as well as along F'2 is shallower and overall larger than along F1, implying clockwise rotation. The small but measurable block rotation is compatible with the bulk dextral shear. On the longer term, this mechanism explains the twisting of the Ziarat fold's western hinge and that of another anticline farther south (Figure 10). Note that the rotation and the block motion between F1, F2-FP, and F'2 are consistent with long-term local "bookshelf faulting" kinematics. This mechanism is named after its resemblance with a stack of books toppling over on a shelf [e.g., Mandl, 1987; Green et al., 2014]. As mentioned above, whatever the scenario (A or B or a combination of both), the kinematics are consistent with a "bookshelf faulting" component.

In fact, both pure and simple shears could be at work within this complex tectonic area. Indeed, the Ziarat fold lies near the core of a tectonic syntaxis, a region where orogenic structures sharply turn around a vertical axis. There are east–west trending folds and faults in the Sulaiman lobe, the north–south oriented folds and fault system of the Kirthar range (e.g., Figure 1), and a right-lateral strike-slip fault system at the western termination of the Sulaiman lobe. The triple junction between these fault systems lies in the tectonic syntaxis that is kinematically unstable, as in a similar context in the core of the NW Himalayan syntaxis [Pécher et al., 2008]. This results in the migration of the Sulaiman lobe's western edge toward the west. It involves a complicated strain field that can only be released by combined localized and distributed deformation [Devès et al., 2011]. The distributed deformation could occur by motion on many small faults within a "damage zone" or "process zone." These terms describe deformation associated with propagating faults [e.g., Cowie and Scholz, 1992; Devès et al., 2011]. The buried multifaults activated during the seismic sequence may participate in these mechanisms, distributing the deformation through a broad right-lateral shear zone. This active shear zone could be restricted to the 15 km wide shear band incorporating the twisted folds to the west and SW of the Ziarat anticline (yellow band in Figure 10). It could also be wider, including the NW trending dextral strike-slip faults east of the Ziarat anticline, such as the Urghargai fault, over a distance of more than 40 km (Figures 1 and 10).

Given its poor surface expression, the affected region appears less mature than others farther east, including the Urghargai fault from Kazmi [1979] as well as two others in the vicinity that offset several geological structures by more than 1.5 km (Figure 10). This suggests either that the fault system activated during the crisis is secondary, or that it is younger. We favor the latter hypothesis which is consistent with a westward migration of the tectonic syntaxis and its associated wrench faults. It is also compatible with the presence in the westernmost part of the shear zone of a "process zone" with a strain field released by combined localized and distributed deformation.

## 6. Conclusion

This study improves understanding of the complex 2008 Ziarat seismic sequence thanks to InSAR. In our interpretation, this sequence mainly involved two previously unrecognized conjugate faults that dissect a major anticline, as well as a 15–20 km long secondary fault and a 10 km long zone affected by tensile cracks. Overall, these structures accommodated ~1 m of westward extrusion of a 50 km<sup>2</sup> rigid block as well as minor clockwise rotation of this block.

The seismic sources are about 15 km to the NW from the epicentral sources suggesting a bias due to the regional velocity model. This result is complementary to and consistent with Weston et al. [2012]. The second main shock, which occurred 12 h after the first main shock, was probably triggered by the unclamping of its fault plane. Farther west, another NE-SW trending shallow sinistral strike-slip fault accommodated 3.5 cm of slip. Based on relative epicentral locations, this latter deformation is likely associated with a precursory earthquake that occurred less than an hour before the first main shock. Three shocks that occurred ~1.5 months later (on 9 December 2008) affected the western termination of the primary NE-SW sinistral fault.

The tectonic sequence as a whole is significantly different from the one postulated based on early analysis of the static stress changes [e.g., McCloskey and Nalbant, 2009; Yadav et al., 2012] and may therefore have different implications for the evaluation of the regional seismic hazard. Furthermore, this tectonic sequence

involved, in the space of a few days, a combination of mechanisms that fits the long-term “escape tectonics” and “bookshelf faulting” concepts. These ideas have been previously proposed to account for the kinematics of areas of distributed deformation. Therefore, the 2008 Ziarat sequence gives a rare opportunity to compare incremental deformation produced at seismic cycle scale with finite deformation on geological timescales. Some of these processes may have important implications for the future evolution of the tectonic syntaxis.

### Acknowledgments

We thank Paul Tapponnier for discussions on bookshelf faulting and Geoffrey C.P. King, M. Simoes, Marie-Pierre Doin, and Belle Philibosian for suggestions. We thank the reviewers for their constructive comments. We also thank the CEA for funding and images. The European Space Agency and the Japanese Aerospace Exploration Agency (JAXA) provided the Envisat and ALOS data, respectively. This is IPGP contribution number 3539.

### References

- Akoglu, A. M., Z. Cakir, M. Meghraoui, S. Belabbes, S. O. El Alami, S. Ergintav, and H. S. Akyüz (2006), The 1994–2004 Al Hoceima (Morocco) earthquake sequence: Conjugate fault ruptures deduced from InSAR, *Earth Planet. Sci. Lett.*, *252*(3), 467–480.
- Ambraseys, N., and R. Bilham (2003), Earthquakes and associated deformation in northern Baluchistan 1892–2001, *Bull. Seismol. Soc. Am.*, *93*(4), 1573–1605.
- Avouac, J. P., F. Ayoub, S. Wei, J. P. Ampuero, L. Meng, S. Leprince, R. Jolivet, Z. Duputel, and D. Helmlinger (2014), The 2013, *Mw* 7.7 Balochistan earthquake, energetic strike-slip reactivation of a thrust fault, *Earth Planet. Sci. Lett.*, *391*, 128–134.
- Bannert, D., F. K. Bender, H. Bender, F. Grüneberg, A. H. Kazmi, H. A. Raza, and F. A. Shams (1995), in *Geology of Pakistan*, Gebrüder borntraeger, Berlin, pp. 1–414.
- Bernard, M., B. Shen-Tu, W. E. Holt, and D. M. Davis (2000), Kinematics of active deformation in the Sulaiman lobe and range, Pakistan, *J. Geophys. Res.*, *105*, 13,253–13,279, doi:10.1029/1999JB900405.
- Bettinelli, P., J.-P. Avouac, M. Flouzat, F. Jouanne, L. Bollinger, P. Willis, and G. R. Chitrakar (2006), Plate motion of India and interseismic strain in the Nepal Himalaya from GPS and DORIS measurements, *J. Geod.*, *80*, 567–589, doi:10.1007/s00190-006-0030-3.
- Biggs, J., E. Bergman, B. Emmerson, G. J. Funning, J. Jackson, B. Parsons, and T. Wright (2006), Fault identification for buried strike-slip earthquakes using InSAR: The 1994 and 2004 Al Hoceima, Morocco earthquakes, *Geophys. J. Int.*, *166*, 1347–1362, doi:10.1111/j.1365-246X.2006.03071.x.
- Cloos, E. (1955), Experimental analysis of fracture patterns, *Bull. Geol. Soc. Am.*, *66*, 241–256.
- Cowie, P. A., and C. H. Scholz (1992), Physical explanation for the displacement-length relationship of faults using a post-yield fracture mechanics model, *J. Struct. Geol.*, *14*, 1133–1148.
- Devès, M., G. C. P. King, Y. Klinger, and A. Agnon (2011), Localised and distributed deformation in the lithosphere: Modelling the Dead Sea region in 3 dimensions, *Earth Planet. Sci. Lett.*, *308*, 172–184.
- Farr, T. G., et al. (2007), The Shuttle Radar Topography Mission, *Rev. Geophys.*, *45*, RG2004, doi:10.1029/2005RG000183.
- Fialko, Y., D. Sandwell, D. Agnew, M. Simons, P. Shearer, and B. Minster (2002), Deformation on nearby faults induced by the 1999 Hector Mine earthquake, *Science*, *297*(5588), 1858–1862.
- Ghiglia, D. C., and L. A. Romero (1994), Robust two-dimensional weighted and unweighted phase unwrapping that uses fast transforms and iterative methods, *J. Opt. Soc. Am. A*, *11*(1), 107–117.
- Goldstein, R. M., and C. L. Werner (1998), Radar interferogram filtering for geophysical applications, *J. Geophys. Res.*, *25*(21), 4035–4038.
- Grandin, R., et al. (2009), September 2005 Manda Hararo Dabbahu rifting event, Afar (Ethiopia): Constraints provided by geodetic data, *J. Geophys. Res.*, *114*, B08404, doi:10.1029/2008JB005843.
- Green, R. G., R. S. White, and T. Greenfield (2014), Motion in the north Iceland volcanic rift zone accommodated by bookshelf faulting, *Nat. Geosci.*, *7*, 29–33.
- Haq, S. S. B., and D. M. Davis (1997), Oblique convergence and the lobate mountain belts of western Pakistan, *Geology*, *25*(1), 23–26.
- Hwang, L. J., and H. Kanamori (1992), Rupture processes of the 1987–1988 Gulf of Alaska earthquake sequence, *J. Geophys. Res.*, *97*(B13), 19,881–19,908, doi:10.1029/92JB01817.
- Jónsson, S., H. Zebker, P. Segall, and F. Amelung (2002), Fault slip distribution of the 1999 *Mw* 7.1 Hector Mine, California, earthquake, estimated from satellite radar and GPS measurements, *Bull. Seismol. Soc. Am.*, *92*, 1377–1389.
- Jouanne, F., A. Awan, A. Madji, A. Pêcher, M. Latif, A. Kausar, J. L. Mugnier, I. Khan, and N. A. Khan (2011), Postseismic deformation in Pakistan after the 8 October 2005 earthquake: Evidence of afterslip along a flat north of the Balakot-Bagh thrust, *J. Geophys. Res.*, *116*, B07401, doi:10.1029/2010JB007903.
- Kazmi, A. H. (1979), Active faults systems in Pakistan, in *Geodynamics of Pakistan*, Geol. Surv. Pak., Quetta, pp. 285–294.
- King, G. C., R. S. Stein, and J. Lin (1994), Static stress changes and the triggering of earthquakes, *Bull. Seismol. Soc. Am.*, *84*, 935–953.
- Larsen, S., R. Reilinger, H. Neugebauer, and W. Strange (1992), Global Positioning System measurements of deformations associated with the 1987 Superstition Hills earthquake: Evidence for conjugate faulting, *J. Geophys. Res.*, *97*(B4), 4885–4902, doi:10.1029/92JB00128.
- Lisa, M., and M. Q. Jan (2010), Geoseismological study of the Ziarat (Balochistan) earthquake (doublet?) of 28 October 2008, *Curr. Sci.*, *98*(1), 50–57.
- Listner, C., J. Goncalves, E. Wolfart, A. Patrono, P. Loreaux, I. Niemeier, A. Ussorio, P. Marpu, and K. H. Gutjar (2010), Integrated analysis of satellite imagery for treaty monitoring: The LIMES experience, *ESARDA Bull.*, *43*, 40–56.
- Mandl, G. (1987), Tectonic deformation by rotating parallel faults: The “bookshelf” mechanism, *Tectonophysics*, *141*, 277–316.
- Maqsood, S. T., and J. Schwarz (2010), Building vulnerability and damage during the 2008 Baluchistan earthquake in Pakistan and past experiences, *Seismol. Res. Lett.*, *81*(3), 514–525.
- Massonnet, D., and K. L. Feigl (1995), Discrimination of geophysical phenomena in satellite radar interferograms, *Geophys. Res. Lett.*, *22*(12), 1537–1540, doi:10.1029/95GL00711.
- McCloskey, J., and S. Nalbant (2009), Near-real-time aftershock hazard maps, *Nat. Geosci.*, *2*, 154–155.
- Meng, L., J. P. Ampuero, J. Stock, Z. Duputel, Y. Luo, and V. C. Tsai (2012), Earthquake in a maze: Compressional rupture branching during the 2012 *Mw* 8.6 Sumatra earthquake, *Science*, *337*(6095), 724–726.
- Molnar, P., and P. Tapponnier (1975), Cenozoic tectonics of Asia – Effects of a continental collision, *Science*, *189*(4201), 419–426.
- Nakata, T., H. Tsutsumi, S. H. Khan, and R. D. Lawrence (1991), *Active Faults of Pakistan: Map Sheets and Inventories, Spec. Publ.*, Research Center for Regional Geography, Hiroshima University, Hiroshima, vol. 21, pp. 1–141.
- Okada, Y. (1985), Surface deformation due to shear and tensile faults in a half-space, *Bull. Seismol. Soc. Am.*, *75*, 1135–1154.
- Okada, Y. (1992), Internal deformation due to shear and tensile faults in a half-space, *Bull. Seismol. Soc. Am.*, *82*(2), 1018–1040.
- Pêcher, A., et al. (2008), Stress field evolution in the northwest Himalayan syntaxis, northern Pakistan, *Tectonics*, *27*, TC6005, doi:10.1029/2007TC002252.
- Pinel-Puysségur, B., R. Michel, and J.-P. Avouac (2012), Multi-link InSAR time series: Enhancement of a wrapped interferometric database, *IEEE J. Sel. Top. Appl. Earth Obs. Remote Sens.*, *5*(3), 784–794, doi:10.1109/JSTARS.2012.2196758.

- PMD report (2009), Seismotectonic analysis of Ziarat, Balochistan earthquake of 29th October, 2008 by Zahid Rafi, Najeeb Ahmed and Shafiq-Ur-Rehman, Technical report no. PMD-32/2009.
- Quittmeyer, R. C., and K. H. Jacob (1979), Historical and Modern Seismicity of Pakistan, Afghanistan, north-western India and southeastern Iran, *Bull. Seismol. Soc. Am.*, *69*, 773–823.
- Robinson, D. P., C. Henry, S. Das, and J. H. Woodhouse (2001), Simultaneous rupture along two conjugate planes of the Wharton Basin earthquake, *Science*, *292*(5519), 1145–1148.
- Sylvester, A. G. (1988), Strike-slip faults, *Geol. Soc. Am. Bull.*, *100*(11), 1666–1703.
- Szeliga, W., R. Bilham, D. Schelling, D. M. Kakar, and S. Lodi (2009), Fold and thrust partitioning in a contracting fold belt: Insights from the 1931 Mach earthquake in Baluchistan, *Tectonics*, *28*, TC5019, doi:10.1029/2008TC002265.
- Szeliga, W., R. Bilham, D. M. Kakar, and S. H. Lodi (2012), Interseismic strain accumulation along the western boundary of the Indian subcontinent, *J. Geophys. Res.*, *117*, B08404, doi:10.1029/2011JB008822.
- Tarantola, A., and B. Valette (1982), Generalized non-linear inverse problems solved using the least squares criterion, *Rev. Geophys. Space Phys.*, *20*, 219–232, doi:10.1029/RG020i002p00219.
- Thatcher, W., and D. P. Hill (1991), Fault orientations in extensional and conjugate strike-slip environments and their implications, *Geology*, *19*(11), 1116–1120.
- Toda, S., and R. Stein (2003), Toggling of seismicity by the 1997 Kagoshima earthquake couplet: A demonstration of time-dependent stress transfer, *J. Geophys. Res.*, *108*(B12), 2567, doi:10.1029/2003JB002527.
- Walker, R. T., E. A. Bergman, J. R. Elliott, E. J. Fielding, A. R. Ghods, M. Ghorashi, and R. J. Walters (2013), The 2010–2011 South Rigan (Baluchestan) earthquake sequence and its implications for distributed deformation and earthquake hazard in southeast Iran, *Geophys. J. Int.*, *193*(1), 349–374.
- West, W. D. (1934), The Baluchistan earthquakes of August 25th and 27th, 1931, *Mem. Geol. Surv. India*, *67*, 1–82.
- Weston, J., A. M. G. Ferreira, and G. J. Funning (2012), Systematic comparisons of earthquake source models determined using InSAR and seismic data, *Tectonophysics*, *532*, 61–81, doi:10.1016/j.tecto.2012.02.001.
- Woessner, J., S. Jónsson, H. Sudhaus, and C. Baumann (2012), Reliability of Coulomb stress changes inferred from correlated uncertainties of finite-fault source models, *J. Geophys. Res.*, *117*, B07303, doi:10.1029/2011JB009121.
- Yadav, R. B. S., V. K. Gahalaut, S. Chopra, and B. Shan (2012), Tectonic implications and seismicity triggering during the 2008 Baluchistan, Pakistan earthquake sequence, *J. Asian Earth Sci.*, *45*, 167–178.